International Journal of Multiphase Flow 101 (2018) 113–124

Contents lists available at ScienceDirect

International Journal of Multiphase Flow

journal homepage: www.elsevier.com/locate/ijmulflow

Application of the Exact Regularized Point Particle method (ERPP) to particle laden turbulent shear flows in the two-way coupling regime

F. Battista*, P. Gualtieri, J.-P. Mollicone, C.M. Casciola

Dipartimento di Ingegneria Meccanica e Aerospaziale, Sapienza Universitá di Roma, Via Eudossiana 18, Roma, 00184, Italy

ARTICLE INFO

Article history:
Received 13 September 2017
Revised 5 January 2018
Accepted 5 January 2018
Available online 11 January 2018

Keywords:
ERPP
Two-way coupling
Turbulence
Accretion disk

ABSTRACT

The Exact Regularized Point Particle method (ERPP), which is a new inter-phase momentum coupling approach, is extensively used for the first time to explore the response of homogeneous shear turbulence in presence of different particle populations. Particle suspensions with different Stokes number and/or mass loading are considered. Particles with Kolmogorov Stokes number of order one suppress turbulent kinetic energy when the mass loading is increased. In contrast, heavier particles leave this observable almost unchanged with respect to the reference uncoupled case. Turbulence modulation is found to be anisotropic, leaving the streamwise velocity fluctuations less affected by unitary Stokes number particles whilst it is increased by heavier particles. The analysis of the energy spectra shows that the turbulence modulation occurs throughout the entire range of resolved scales leading to non-trivial augmentation/depletion of the energy content among the different velocity components at different length-scales. In this regard, the ERPP approach is able to provide convergent statistics up to the smallest dissipative scales of the flow, giving the opportunity to trust the ensuing results. Indeed, a substantial modification of the turbulent fluctuations at the smallest-scales, i.e. at the level of the velocity gradients, is observed due to the particle backreaction. Small scale anisotropies are enhanced and fluctuations show a greater level of intermittency as measured by the probability distribution function of the longitudinal velocity increments and by the corresponding flatness.

1. Introduction

Turbulent multiphase flows consist in a carrier fluid transporting a disperse phase typically represented by solid particles, small liquid droplets or gas bubbles. In many circumstances, ranging from natural phenomena, see e.g. (Woods, 2010; Fu et al., 2014; Durham et al., 2013), to technological applications, see e.g. (Post and Abraham, 2002; Hoef et al., 2008), the carrier flow is turbulent and advects the disperse phase which in turns can modify the carrier flow itself.

Particle-laden turbulent flows have been well understood in the so-called one-way coupling regime where the mass of the transported phase is much smaller than the mass of the carrier phase so that the carrier flow is not altered by the particles. In these conditions, when the particle relaxation timescale τ_p is of the order of the Kolmogorov timescale τ_η, solid particles form small scale aggregates known as clusters, see e.g. (Reade and Collins, 2000; Monchaux et al., 2010; Bec et al., 2007; Yoshimoto and Goto, 2007; Saw et al., 2008; Toschi and Bodenschatz, 2009; Meneguz and Reeks, 2011; Calzavarini et al., 2008; Salazar et al., 2008) among many. When the particles are transported by anisotropic flows, the clusters show a directionality induced by the mean velocity gradient as documented by Shotorban and Balachandar (2006); Gualtieri et al. (2009) and Nicolai et al. (2013) in the context of homogeneous shear turbulence, see also (Nicolai et al., 2014) where a comparison between experimental and numerical data can be found. The same issue was addressed by Pitton et al. (2012) in the case of a channel flow and Poelma et al. (2007) in the case of grid-generated turbulence. Preferential spatial aggregation is also observed in inhomogeneous flows. For instance, in wall bounded flows, the particles tend to segregate in the near-wall region. This phenomenon, known as turbophoresis, (Caporaloni et al., 1975) and Young and Leeming (1997), has been widely studied in planar channels, (Reeks, 1983; Marchioli et al., 2007), pipes, (Vreman, 2007; Picano et al., 2009; Soldati and Marchioli, 2009), spatially developing flows such as boundary layers, (Marchioli and Soldati, 2002; Sardina et al., 2012; Li et al., 2016), turbulent jets, (Longmire and Eaton, 1992; Picano et al., 2010; Li et al., 2011; Lau and Nathan, 2016) reactive flows, (Battista et al., 2011) and mixing-layers in

* Corresponding author.
E-mail address: francesco.battista@uniroma1.it (F. Battista).

https://doi.org/10.1016/j.ijmultiphaseflow.2018.01.006

presence of evaporation both in the context of DNS (Miller and Bellan, 1999; Okongo and Bellan, 2004) and LES (Leboissetier et al., 2005) simulations. These issues are certainly relevant for modeling purposes in the context of Reynolds Averaged Navier Stokes (RANS) approaches (Peirano et al., 2006; Meyer, 2012), and for Large Eddy Simulations (LES) (Marchioli et al., 2008; Innocenti et al., 2016), see also the recent review by Marchioli (2017).

The one-way coupling assumption oversimplifies reality when the mass loading of the suspension is no more negligible. In many applications, the inter-phase momentum exchange must be taken into account in a regime where the inter-particle collisions and the hydrodynamic interactions can be still neglected. These circumstances occur when the volume fraction of the suspension Φ_V is small (dilute suspension) but the solid-to-fluid density ratio ρ_p/ρ_f is large, resulting in a mass loading $\Phi = \left(\rho_p/\rho_f\right)\Phi_V$ of order one. At the same time, the disperse phase can still be modeled as an ensemble of small spheres (diameter d_p smaller than the Kolmogorov dissipative scale η). In the so-called two-way coupling regime, the disperse phase back-reacts on the carrier fluid. The turbulence modulation, in turn, produces a modified advection of the suspension, see e.g. (Elghobashi, 1994; Elgobashi, 2006) for a discussion of the different transport regimes and the review papers by Crowe et al. (1996); Balachandar and Eaton (2010) where a large literature survey can be found.

The numerical modeling of the inter-phase momentum coupling is a major concern in numerical simulations when the transported phase is disperse and formed by huge number of tiny particles. In fact, the sparse and relatively small ($d_p \ll \eta$) particles must be followed by a classic Lagrangian, point-wise approach. In contrast, the fluid must be treated by a standard Eulerian description. This unavoidable asymmetry is the cause of two difficulties. The first one consists of the mismatch between particle positions and nodes of the Eulerian grid, that calls for numerical interpolation from particles to Eulerian grid and vice versa. This issue, though relevant, see (Balachandar and Maxey, 1989), is not the focus of the present paper and will not be pursued further. The second and, in our opinion, most important difficulty is that the particles represent localized sources of momentum for the fluid. The carrier phase is forced by such concentrated, singular forces that need to be suitably regularized to be effective for the numerical solution of the carrier flow. The Particle In Cell (PIC) method introduced by Crowe et al. (1977) exploits spatial averaging across the computational cell occupied by the particle to smooth the back-reaction field out, see e.g. among many (Ferrante and Elghobashi, 2003; Gualtieri et al., 2013) or (Zhao et al., 2010) for applications to homogeneous isotropic turbulence, turbulent homogeneous shear flow or turbulent channel flow, respectively. There are drawbacks, however, since this averaging procedure lacks a clear physical interpretation and is grid dependent, see the review by Eaton (2009) and the discussion reported in Boivin et al. (1998); Garg et al. (2007); Gualtieri et al. (2013). The issue becomes particularly crucial for highly uneven distributions of particles, as occurring in turbulent sprays (Marmottant and Villermaux, 2004; Jenny et al., 2012). Recently, it was highlighted by several authors that the calculation of the hydrodynamic force on the particles is another crucial issue in Euler-Lagrangian simulations of particle laden flows in the two-way coupling regime. Indeed, the fluid velocity at the particle position that enters in the expression of the hydrodynamic force, must be understood as the undisturbed flow, i.e. the flow that one would have if the particle in question had no effect on the flow. These circumstances are hardly achieved in two-way coupled simulations, where the particle locally modifies the flow calling for a procedure aimed at removing only the spurious self-disturbance and retaining the effects of all the other particles. To this purpose, (Horwitz and Mani, 2016; 2017) developed and validated an accurate numerical interpolation procedure to remove the particle self-disturbance in the context of PIC simulations. The authors were able to correctly estimate the force on the particle by adding a proper correction of the fluid velocity evaluated at the particle position. Akiki et al. (2017) addressed the effects of the local volume fraction. When the particles are unevenly distributed, the effect of the disturbance flow due to surrounding neighbors must be taken into account in the expression of the hydrodynamic force. The authors consider a proper background flow which accounts for the disturbance flow due to the surrounding neighbors. The approach is particularly efficient since it exploits precomputed pairwise particle hydrodynamic interactions. Alternative methods exploits volume-filtered Eulerian–Lagrangian approaches, see (Capecelatro and Desjardins, 2013), where the inter-phase momentum coupling is achieved by filtering the equations of motion on scales much larger than the scale of the particles and providing appropriate models for the unclosed terms. Ireland and Desjardins (2017) highlighted once more the need to remove the self-disturbance flow in the expression of the hydrodynamic force. The authors present a new strategy to evaluate the undisturbed flow at the particle position by introducing a proper filtering procedure. The results are validated in the case of a particle settling under the effect of gravity. It is worth stressing that this test is particularly challenging in two-way coupled simulations since the self-disturbance must be properly removed if one wishes to capture the correct terminal velocity of the particle.

The present paper deals with the Direct Numerical Simulation (DNS) of particle laden turbulent flows in the two-way coupling regime in the geometrical configuration of the homogeneous shear flow (HSF). The HSF configuration is ideal to address fundamental issues of turbulent modulation and serves as prototypal flow with respect to more complex wall-bounded flows where the spatial non-homogeneity might hinder the statistical analysis and overcomes some drawbacks of homogeneous isotropic turbulence. Particle clusters are elongated spanning from the integral to the dissipative scale. It follows that the back-reaction is active across the entire spectrum of scales. In homogenous isotropic turbulence, an external forcing is usually applied to the largest scales to keep the flow statistically steady. In such case the forcing directly modifies the large scale features of the clusters, leading to unphysical effects, since external forcing and flow should be statistically independent, whereas particle forcing is strongly correlated with the flow. On the other hand, the HSF self-sustains fluctuations, implying that clusters consistently affect the flow itself. The HSF is therefore among the simplest (if not the simplest) of flows where particle-fluid interactions can be addressed with no artefact. The fluid/particle coupling is modeled using the Exact Regularized Point Particle (ERPP) method, presented in Gualtieri et al. (2015), which overcomes the drawbacks of the classical PIC approach whilst preserving computational efficiency. The ERPP approach was proved to give convergent statistics up to the smallest dissipative scales of the flow, see e.g. (Gualtieri et al., 2017), giving the opportunity to trust the ensuing results. The study in Gualtieri et al. (2017), however, addressed only one issue, i.e. the energy spectrum modification, due to a specific particle population and was not conceived to give a full characterization of the turbulence modification when the control parameters, namely the Stokes number and the mass loading, are concurrently changed. The present paper fills this gap and provides a complete characterization of the turbulent modification when different particle populations are considered. A wide region of the control parameter space is explored by addressing particles with three different Stokes numbers ($St_\eta = 0.3, 1, 5$) and three different mass loadings ($\phi = 0.2, 0.4, 0.8$). As revealed by single point statistics, i.e. the turbulent kinetic energy and the variances of the single velocity components, the turbulence modulation results to be anisotropic. The streamwise velocity fluctuations are less affected by unitary Stokes

number particles whilst they are increased by heavier particles. In contrast, cross-flow velocity components show a depletion with increasing mass loading, irrespective of the Stokes number. The analysis of the energy spectra which can be successfully performed in homogeneous conditions, show that the turbulence modulation occurs throughout the entire range of resolved scales leading to non-trivial augmentation/depletion of the energy contents among the different velocity components at different length-scales. A substantial modification of the turbulent fluctuations at the smallest-scales (at the level of the velocity gradients) is observed due to the particle backreaction. Small-scale anisotropies are enhanced, as measured by the statistics of the pseudo dissipation tensor. This result calls for a more accurate study of the small-scale statistics of the turbulent fluctuations in the two-way coupling regime. The probability distribution function of the longitudinal velocity increments measured at small separation (comparable with the Kolmogorov scale) show a substantial broadening, under specific conditions, with respect to the one-way coupling case. Thus, intermittency is increased by the particle backreaction as measured by the corresponding flatness.

The paper is organized as follows: Section 2 provides a brief survey of the Exact Regularized Point Particle (ERPP) method. Section 3 addresses the results of two-way coupled simulations of the homogeneous particle-laden turbulent shear flow by presenting both single point Eulerian statistics and energy spectra. Section 4 summarizes the results of our study and its potentials for the DNS of particle-laden turbulent flows.

2. Momentum coupling model

This section summarizes the physical model used to achieve the inter-phase momentum coupling between the carrier fluid and the disperse phase. The reader can refer to Gualtieri et al. (2015) for a detailed discussion of the methodology.

2.1. Carrier phase

The fluid-particle interaction occurs via the non-slip boundary condition enforced at each particle boundary. The carrier fluid fills the domain $\mathcal{D}\backslash\Omega$ where $\mathcal{D}$ is the flow domain and $\Omega(t)=\cup_p\Omega_p(t)$ denotes the region occupied by the collection of N_p rigid particles, with $\Omega_p(t)$ the time dependent domain occupied by the pth particle. The motion of the carrier fluid is described by the incompressible Navier–Stokes equations equipped with the no-slip condition at the particle boundaries

$$\left.\begin{aligned}&\nabla\cdot\mathbf{u}=0\\&\frac{\partial\mathbf{u}}{\partial t}+\mathbf{u}\cdot\nabla\mathbf{u}=-\frac{1}{\rho_f}\nabla \mathrm{p}+\nu\nabla^2\mathbf{u}\end{aligned}\right\}\qquad \mathbf{x}\in\mathcal{D}\backslash\Omega(t)$$
$$\begin{aligned}&\mathbf{u}|_{\partial\Omega_p(t)}=\mathbf{v}_p(\mathbf{x})|_{\partial\Omega_p(t)}\qquad p=1,\dots,N_p\\&\mathbf{u}|_{\partial\mathcal{D}}=\mathbf{u}_{wall}\\&\mathbf{u}(\mathbf{x},0)=\mathbf{u}_0(\mathbf{x})\qquad \mathbf{x}\in\mathcal{D}\backslash\Omega(0)\ .\end{aligned}\tag{1}$$

In Eq. (1), $\mathbf{u}_0(\mathbf{x})$ is the velocity field at time $t=0$, ρ_f denotes the fluid density, ν is the kinematic viscosity, and $\mathbf{v}_p(\mathbf{x})$ the velocity of the particle boundary. In principle, the system can be numerically integrated at the price of resolving all the particle boundaries on the computational grid. However, when the carrier flow is laden by a huge number of small particles, a direct solution strategy is unaffordable. The idea is to relocate the boundary condition at the particle surface on a properly defined correction flow field which, in the limit of small particles, is amenable of an analytical solution. To this purpose the carrier fluid velocity $\mathbf{u}$ is decomposed into two parts, $\mathbf{u}(\mathbf{x},t)=\mathbf{w}+\mathbf{v}$ where the (background) field $\mathbf{w}(\mathbf{x},t)$ is assumed to satisfy the equations

$$\begin{aligned}&\nabla\cdot\mathbf{w}=0\\&\frac{\partial\mathbf{w}}{\partial t}+\mathbf{F}=-\frac{1}{\rho_f}\nabla\pi+\nu\nabla^2\mathbf{w}\\&\mathbf{w}|_{\partial\mathcal{D}}=\mathbf{u}_{wall}-\mathbf{v}_{\partial\mathcal{D}}\\&\mathbf{w}(\mathbf{x},0)=\tilde{\mathbf{u}}_0(\mathbf{x}),\end{aligned}\tag{2}$$

where $\mathbf{x}\in\mathcal{D}$ and

$$\mathbf{F}=\begin{cases}\mathbf{u}\cdot\nabla\mathbf{u} & \text{for } \mathbf{x}\in\mathcal{D}\backslash\Omega(t)\\ \mathbf{v}_p\cdot\nabla\mathbf{v}_p & \text{for } \mathbf{x}\in\Omega(t)\end{cases}\tag{3}$$

is a field reproducing the complete convective term of the Navier–Stokes equation in the carrier fluid domain $\mathcal{D}\backslash\Omega$ which is prolonged inside Ω using the rigid-body particle velocity. In Eq. (2), the convective term retains its complete nonlinear nature in the fluid domain and is treated as a prescribed forcing term. The no-slip boundary condition at the particle surface has been removed even though the particles still affect the field trough the boundary condition enforced on $\partial\mathcal{D}$. The non-slip boundary condition at the particle surface is recovered when considering the particle perturbation field $\mathbf{v}(\mathbf{x},t)$ which exactly satisfies the *linear* unsteady Stokes problem (the complete non-linear term has been retained in the equation for $\mathbf{w}$)

$$\left.\begin{aligned}&\nabla\cdot\mathbf{v}=0\\&\frac{\partial\mathbf{v}}{\partial t}=-\frac{1}{\rho_f}\nabla \mathrm{q}+\nu\nabla^2\mathbf{v}\end{aligned}\right\}\qquad \mathbf{x}\in\mathcal{D}\backslash\Omega(t)$$
$$\begin{aligned}&\mathbf{v}|_{\partial\Omega_p(t)}=\mathbf{v}_p(\mathbf{x})|_{\partial\Omega_p(t)}-\mathbf{w}|_{\partial\Omega_p(t)}\qquad p=1,\dots N_p\\&\mathbf{v}(\mathbf{x},0)=0\qquad \mathbf{x}\in\mathcal{D}\backslash\Omega(0).\end{aligned}\tag{4}$$

The solution of Eq. (4) can be expressed in terms of the boundary integral representation of the unsteady Stokes equations, see e.g. classical textbooks, (Happel and Brenner, 2012). In the limit of small particle diameter d_p, the far field disturbance flow can be estimated in terms of a multipole expansion of the complete solution, namely

$$v_i(\mathbf{x},t)=-\sum_p\int_0^t D_j^p(\tau)G_{ij}(\mathbf{x},\mathbf{x}_p,t,\tau)\,d\tau\,,\tag{5}$$

where $G_{ij}(\mathbf{x},\boldsymbol{\xi},t,\tau)$ is the so called unsteady Stokeslet which is interpreted as the fluid velocity (ith direction) at position $\mathbf{x}$ and time t due to the singular forcing $\delta(\mathbf{x}-\boldsymbol{\xi})\delta(t-\tau)$ (jth direction) applied at point $\boldsymbol{\xi}$ and at time τ. Eq. (5) shows that the far field disturbance depends only on the hydrodynamic force $\mathbf{D}_p(\tau)$, with Cartesian components D_j^p, which acts on the generic particle. Since the unsteady Stokeslet G_{ij} solves the singularly forced unsteady Stokes problem, the partial differential equation whose solution is given by (5) follows as

$$\begin{aligned}&\frac{\partial\mathbf{v}}{\partial t}-\nu\nabla^2\mathbf{v}+\frac{1}{\rho_f}\nabla \mathrm{q}=-\frac{1}{\rho_f}\sum_p\mathbf{D}_p(t)\,\delta[\mathbf{x}-\mathbf{x}_p(t)];\\&\mathbf{v}(\mathbf{x},0)=0,\end{aligned}\tag{6}$$

In Eq. (6), the fluid-particle coupling occurs via the (singular) forcing term in the unsteady Stokes problem. Coming back to Eq. (2): as the particle diameter vanishes, the term $\mathbf{F}$ uniformly fills the entire domain $\mathcal{D}$ and reduces almost everywhere to the standard convective term of the Navier–Stokes equation $\mathbf{u}\cdot\nabla\mathbf{u}$.

The crucial step for a practical and efficient numerical solution of the particle-laden flow consists in regularising the solution of Eq. (6). This can be achieved by thinking in terms of the associated vorticity field $\boldsymbol{\zeta}=\nabla\times\mathbf{v}$ which obeys a (vector) diffusion equation whose solution can be expressed as a convolution with the fundamental solution of the diffusion equation $g(\mathbf{x}-\boldsymbol{\xi},t-\tau)$ that is a Gaussian with time dependent variance $\sigma(t-\tau)=\sqrt{2\nu(t-\tau)}$.

By rearranging the forcing on the right hand side of Eq. (6) as a time-convolution, the solution for the vorticity field follows as

$$\boldsymbol{\zeta}(\mathbf{x},t)=\frac{1}{\rho_f}\int_0^{t^+}\mathbf{D}_p(\tau)\times\nabla g[\mathbf{x}-\mathbf{x}_p(\tau),t-\tau]d\tau\ . \tag{7}$$

The disturbance vorticity field $\boldsymbol{\zeta}$ is still singular, with singularity arising from the contribution to the integral near the upper integration limit, $\tau\simeq t$. However, away from the upper integration limit, the integrand is regular since it involves a Gaussian or its gradient. This observation can be exploited to define a regularization procedure based on a temporal cut-off ϵ_R such that the field is additively split into a regular and a singular component, $\boldsymbol{\zeta}(\mathbf{x},t)=\boldsymbol{\zeta}_R(\mathbf{x},t;\epsilon_R)+\boldsymbol{\zeta}_S(\mathbf{x},t;\epsilon_R)$, where the regular component is given by

$$\boldsymbol{\zeta}_R(\mathbf{x},t)=\frac{1}{\rho_f}\int_0^{t-\epsilon_R}\mathbf{D}_p(\tau)\times\nabla g[\mathbf{x}-\mathbf{x}_p(\tau),t-\tau]d\tau\ . \tag{8}$$

As implied by the fundamental solution for the diffusion equation, the regular part of the vorticity field is everywhere smooth and characterized by the smallest spatial scale $\sigma_R=\sigma(\epsilon_R)=\sqrt{2\nu\epsilon_R}$. The corresponding vorticity field $\boldsymbol{\zeta}_R$ at time t obeys a forced diffusion equation where the forcing is applied at the slightly earlier time $t-\epsilon_R$,

$$\frac{\partial\boldsymbol{\zeta}_R}{\partial t}-\nu\nabla^2\boldsymbol{\zeta}_R=-\frac{1}{\rho_f}\nabla\times\mathbf{D}_p(t-\epsilon_R)g[\mathbf{x}-\mathbf{x}_p(t-\epsilon_R),\epsilon_R]$$
$$\boldsymbol{\zeta}_R(\mathbf{x},0)=0\,. \tag{9}$$

The complete regularized field, on the other hand, obeys the forced unsteady Stokes equation

$$\frac{\partial\mathbf{v}_R}{\partial t}-\nu\nabla^2\mathbf{v}_R+\frac{1}{\rho_f}\nabla\mathrm{q}_R$$
$$=-\frac{1}{\rho_f}\mathbf{D}_p(t-\epsilon_R)\,g[\mathbf{x}-\mathbf{x}_p(t-\epsilon_R),\epsilon_R] \tag{10}$$

for the solenoidal field $\mathbf{v}_R$ that can be split in terms of a pseudo-velocity,

$$\frac{\partial\mathbf{v}_{\boldsymbol{\zeta}_R}}{\partial t}-\nu\nabla^2\mathbf{v}_{\boldsymbol{\zeta}_R}=-\frac{1}{\rho_f}\mathbf{D}_p(t-\epsilon_R)\,g[\mathbf{x}-\mathbf{x}_p(t-\epsilon_R),\epsilon_R] \tag{11}$$

governed by the unsteady diffusion operator plus a correction required to enforce solenoidality, $\mathbf{v}_R=\mathbf{v}_{\boldsymbol{\zeta}_R}+\nabla\phi_R$. Note that both the regularized correction and the regularized pseudo-velocity are forced by the anticipated Stokes drag (i.e. evaluated at $t-\epsilon_R$) times the regular spatial distribution $g[\mathbf{x}-\mathbf{x}_p(t-\epsilon_R),\epsilon_R]$ which makes the pseudo-velocity an extremely localized field, since it involves the diffusion of the localized source for a short time interval ϵ_R.

In contrast to $\mathbf{v}_R$, the singular contribution $\mathbf{v}_S$ cannot be represented on a discrete grid. However, it can be shown that its contribution is of the order of the particle Reynolds number and can be thus neglected, see (Gualtieri et al., 2015) for details. In any case, this highly localized field will eventually diffuse to larger scales at later times. The singular contribution that is neglected during a single time step is successively reintroduced in the field as soon as it reaches the smallest physically relevant scales of the system.

The regularized fluid velocity of the carrier flow in presence of the particles can be obtained by aggregating the two contributions of the velocity decomposition $\mathbf{u}=\mathbf{w}+\mathbf{v}_R$. Once the contribution arising from the singular perturbation field $\mathbf{v}_S$ is neglected, the equations for the fluid field $\mathbf{u}$ read

$$\nabla\cdot\mathbf{u}=0$$
$$\frac{\partial\mathbf{u}}{\partial t}+\mathbf{u}\cdot\nabla\mathbf{u}=-\frac{1}{\rho_f}\nabla p+\nu\nabla^2\mathbf{u}$$
$$-\frac{1}{\rho_f}\sum_p^{N_p}\mathbf{D}_p(t-\epsilon_R)\,g[\mathbf{x}-\mathbf{x}_p(t-\epsilon_R),\epsilon_R]\ . \tag{12}$$

where we have added the contributions arising from all the N_p particles transported by the fluid. The above set of equations simply state that along its motion the particles experience a concentrated hydrodynamic force which, in turns, acts on the fluid via its regularized form. In the proposed model, the regularization is naturally provided by the viscous diffusion and thus does not require any *ad-hoc* numerical artefact. The effect of the hydrodynamic force is the generation of the regularized vorticity field, Eq. (8), that is characterized by the smallest length-scale $\sigma_R=\sqrt{2\nu\epsilon_R}$ where ϵ_R is the regularization diffusion timescale. The net effect of the disperse phase on the regularized carrier flow field is then accounted for by the extra forcing term which involves the time-delayed hydrodynamic force $\mathbf{D}_p(t-\epsilon_R)$ and the Gaussian $g[\mathbf{x}-\mathbf{x}_p(t-\epsilon_R),\epsilon_R]$ with variance σ_R. In a turbulent flow laden with sub-Kolmogorov sized particles, the interest is on the net effects that the swarm of particles have on the resolved turbulent scales. It follows that the regularization length-scale can be immediately chosen as $\sigma_R=\eta$.

Even though the formal derivation of the momentum coupling model might result cumbersome under the mathematical point of view, the equations that must be solved are straightforward. Any standard Navier–Stokes solver can be easily equipped with an extra term which is known in closed form. Moreover, each particle produces an active forcing on the fluid localized in a sphere of radius order σ_R centred at the particle position. In presence of many particles, only the few grid points in the sphere of influence of each particle need to be updated. In a nutshell, the forcing decays more than exponentially in space allowing to achieve highly efficient numerical algorithms which allow to tackle the effect of millions of small particles.

2.2. Disperse phase

The disperse phase consists of small spherical particles of diameter d_p that can be considered as material points of mass m_p. Their evolution follows the standard Newton's law

$$\frac{d\mathbf{x}_p}{dt}=\mathbf{v}_p(t),\quad m_p\frac{d\mathbf{v}_p}{dt}=\mathbf{D}_p(t)+\big(m_p-m_f\big)\mathbf{g}, \tag{13}$$

where m_f is the mass of the displaced fluid, $\mathbf{D}_p(t)$ is the hydrodynamic force, and $\mathbf{g}$ the acceleration due to gravity. For inertial particles, $\rho_p\gg\rho_f$, the hydrodynamic force reduces to the Stokes drag, see e.g. (Maxey and Riley, 1983; Gatignol, 1983; Olivieri et al., 2014),

$$\mathbf{D}_p(t)=6\pi\mu a_p[\tilde{\mathbf{u}}(\mathbf{x}_p,t)-\mathbf{v}_p(t)]\,, \tag{14}$$

where $a_p=d_p/2$ is the particle radius and μ the dynamic viscosity. The expression of the force holds in the limit of vanishing particle Reynolds number defined as $Re_p=||\mathbf{u}|_p-\mathbf{v}_p||\,d_p/\nu$. The probability density function (PDF) of the particle Reynolds number is shown in Fig.1 for a few of the cases reported in Table 1. The PDF shows a definite peak that is well below the critical value of $Re_p=1$. The tails rapidly drop as $Re_p\to1$, confirming that irrespective of the particle diameter (Stokes number), all the particles of a specific population can be considered to be in the Stokes regime. Following the original derivation provided in Maxey and Riley (1983); Gatignol (1983), the velocity $\tilde{\mathbf{u}}(\mathbf{x}_p,t)$ differs from $\mathbf{u}(\mathbf{x}_p,t)$ and must be interpreted as the fluid velocity at the particle position in absence of the particle self-interaction. That is, $\tilde{\mathbf{u}}_p$ should account for the background turbulent flow and for the disturbance generated by all the other particles except the pth one. In the two-way coupling regime, where the particle back-reaction modifies the carrier flow, the correct and efficient calculation of $\tilde{\mathbf{u}}_p$ is crucial and calls for an effective procedure to remove the particle self-interaction contribution at the particle position from the field $\mathbf{u}$. The ERPP approach allows to purge the spurious self-induced contribution since the disturbance flow generated by each particle can be easily evaluated in closed form. More specifically, the self-disturbance

Table 1
Simulations matrix.
The Navier–Stokes equations are integrated in a $4\pi \times 2\pi \times 2\pi$ periodic box with a resolution of $N_x \times N_y \times N_z$ collocation points in physical space. For all cases, the shear parameter is $S^* = 7$. The Taylor Reynolds number is $Re_\lambda = u_{rms}\lambda/\nu$, N_p denotes the number of particles and Φ is the mass loading (see text for definitions). The Stokes number is defined as $St_\eta = \tau_p/\tau_\eta$ where τ_η is the Kolmogorov time. The ratio between the disperse and carrier phase densities is ρ_p/ρ_f. The dataset is organized into four sections. The first three entries, A_1, B_1, C_1, provide realistic cases with few particles per cell to be compared with cases A_2, B_2 and C_2 where the average number of particles per cell is intentionally made unitary at the expense of having an unrealistic density ratio. The last six entries, *D, E, F,* E_1, E_2 and E_3, provide data at relatively higher Reynolds number and at different Stokes numbers. In all cases, the regularization length-scale σ_R is chosen to match the Kolmogorov scale η and the grid spacing is such that $Dx = \eta$. Entries B_3 and B_4 serve for numerical purposes to assess the independency of the results under grid refinement in case B_3 where $Dx/\eta = 0.5$; $\sigma_R/\eta = 1$ and for changes of the regularization length-scale in case B_4 where $Dx/\eta = 0.5$; $\sigma_R/\eta = 0.5$. The regularization time scale ϵ_R can be found for all cases through the relation $\epsilon_R/\tau_\eta = 0.5(\sigma_R/\eta)^2$.

Case	N	Re_λ	N_p	Φ	ρ_p/ρ_f	St_η	d_p/η	σ_R/η	Dx/η
A_1	288 x 288 x 144	55	297.760	0.2	1800	1	0.1	1	1
B_1	288 x 288 x 144	55	595.520	0.4	1800	1	0.1	1	1
C_1	288 x 288 x 144	55	1.191.040	0.8	1800	1	0.1	1	1
A_2	288 x 288 x 144	55	1.769.472	0.2	63500	1	0.017	1	1
B_2	288 x 288 x 144	55	1.769.472	0.4	13600	1	0.036	1	1
C_2	288 x 288 x 144	55	1.769.472	0.8	3690	1	0.07	1	1
B_3	576 x 576 x 288	55	595.520	0.4	1800	1	0.1	1	0.5
B_4	576 x 576 x 288	55	595.520	0.4	1800	1	0.1	0.5	0.5
D	384 x 384 x 192	80	1.100.000	0.2	1800	1	0.1	1	1
E	384 x 384 x 192	80	2.200.000	0.4	1800	1	0.1	1	1
F	384 x 384 x 192	80	4.400.000	0.8	1800	1	0.1	1	1
E_1	384 x 384 x 192	80	440.000	0.4	9000	5	0.1	1	1
E_2	384 x 384 x 192	80	196.500	0.4	1800	5	0.23	1	1
E_3	384 x 384 x 192	80	3.111.270	0.4	100	0.3	0.23	1	1

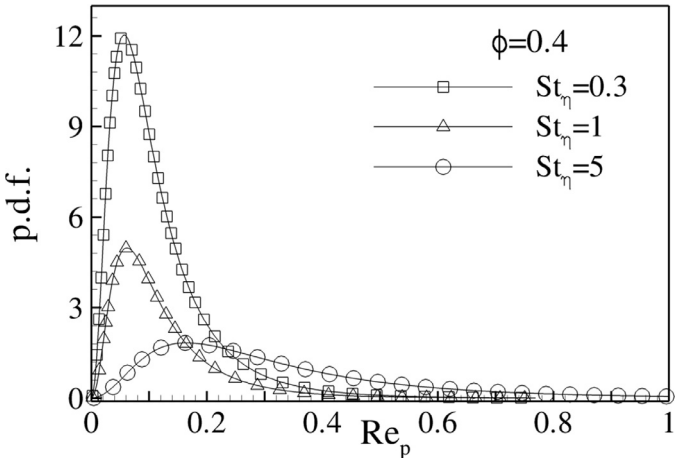

Fig. 1. Probability density function of the particle Reynolds number, see text for definition, for fixed mass loading $\phi = 0.4$ and three different particle populations: $St_\eta = 0.3$ (□); $St_\eta = 1$ (△); $St_\eta = 5$ (○).

field produced by the pth particle in a time step $t_n \to t_{n+1}$ can be derived by integrating the complete equation for the disturbance, namely Eq. (10) with the initial condition $\mathbf{v}(\mathbf{x}, t_n) = 0$. For the illustrative case of the Euler time integration, the solution $\mathbf{v}(\mathbf{x}, t_{n+1})$ is achieved by splitting the operator in (10) into three steps: the forcing step, the diffusion step and the projection step which enforces the divergence-free constraint. Note that the same procedure holds for each sub-step in a generic Runge–Kutta method. The detailed calculations, see e.g. (Gualtieri et al., 2015), lead to the closed form expression of the self-disturbance velocity field

$$\mathbf{v}_{R,p}(\mathbf{x}, t_{n+1}) = \frac{1}{\left(2\pi\sigma^2\right)^{3/2}}\left\{\left[e^{-\eta^2} - \frac{f(\eta)}{2\eta^3}\right]\mathbf{D}_p^n - \left(\mathbf{D}_p^n \cdot \hat{\mathbf{r}}\right)\left[e^{-\eta^2} - \frac{3f(\eta)}{2\eta^3}\right]\hat{\mathbf{r}}\right\}, \tag{15}$$

where we have defined $\mathbf{D}_p^n = \mathbf{D}_p(t_n - \epsilon_R)$, $\mathbf{r} = \mathbf{x} - \mathbf{x}_p(t_n - \epsilon_R)$, the hat denotes $\hat{\mathbf{r}} = \mathbf{r}/r$, $\eta = r/\sqrt{2}\sigma$ is the dimensionless distance with $\sigma = \sqrt{2\nu(\epsilon_R + \Delta t)}$ and $f(\eta) = \frac{\sqrt{\pi}}{2}\mathrm{erf}(\eta) - \eta e^{-\eta^2}$. The value $\mathbf{v}_{R,p}[(\mathbf{x}_p(t_{n+1}), t_{n+1})]$ is then used to compute $\tilde{\mathbf{u}}_p[\mathbf{x}_p(t_{n+1}), t_{n+1})] = \mathbf{u}_p[\mathbf{x}_p(t_{n+1}), t_{n+1})] - \mathbf{v}_{R,p}[(\mathbf{x}_p(t_{n+1}), t_{n+1})]$.

3. Results and discussion

The following sections discuss the turbulence modification due to different particle populations in the homogenous shear flow (HSF). Section 3.1 summarizes the dataset. In Section 3.2, the alteration of single-point statistics such as the turbulent kinetic energy is presented. The third Section 3.3 concerns the modification of energy and dissipation spectra. The last Section 3.4 addresses the anisotropic turbulent modification and the alteration of turbulence intermittency.

3.1. Homogeneous shear flow & dataset

The homogeneous shear flow is a turbulent flow in a periodic box with an imposed mean flow $\mathbf{U} = Sx_2\mathbf{e}_1$ in the streamwise direction $\mathbf{e}_1$. The direction $\mathbf{e}_2$ is along the mean (constant) shear S and $\mathbf{e}_3$ denotes the spanwise coordinate. The coordinates along $\mathbf{e}_1$, $\mathbf{e}_2$ and $\mathbf{e}_3$ will be denoted as $(x_1, x_2, x_3) = (x, y, z)$. The mean shear S extracts energy from the mean flow and forces turbulent fluctuations via the Reynolds shear stress as seen in a planar channel, pipe or turbulent jet. This mechanism results in an anisotropic forcing of the largest scales. On dimensional ground, the turbulence is characterized by two dimensionless parameters, namely the Corrsin parameter S_c^* and the shear strength S^*. The Corrsin parameter, defined as $S_c^* = S(\nu/\epsilon)^{1/2} = (\eta/L_S)^{2/3}$, η being the Kolmogorov scale, $L_S = \sqrt{\epsilon/S^3}$ the shear scale and ϵ the energy dissipation rate, can be recast in terms of the Taylor-Reynolds number $1/S_c^* \propto \mathrm{Re}_\lambda = u_{rms}\lambda/\nu$, where $u_{rms} = \sqrt{\langle u_i u_i\rangle/3}$ is root mean square value of the velocity fluctuations, with u_i as the i^{th} Cartesian component of the velocity fluctuation and the angular brackets denoting ensemble averaging, and λ is the Taylor scale. The Corrsin pa-

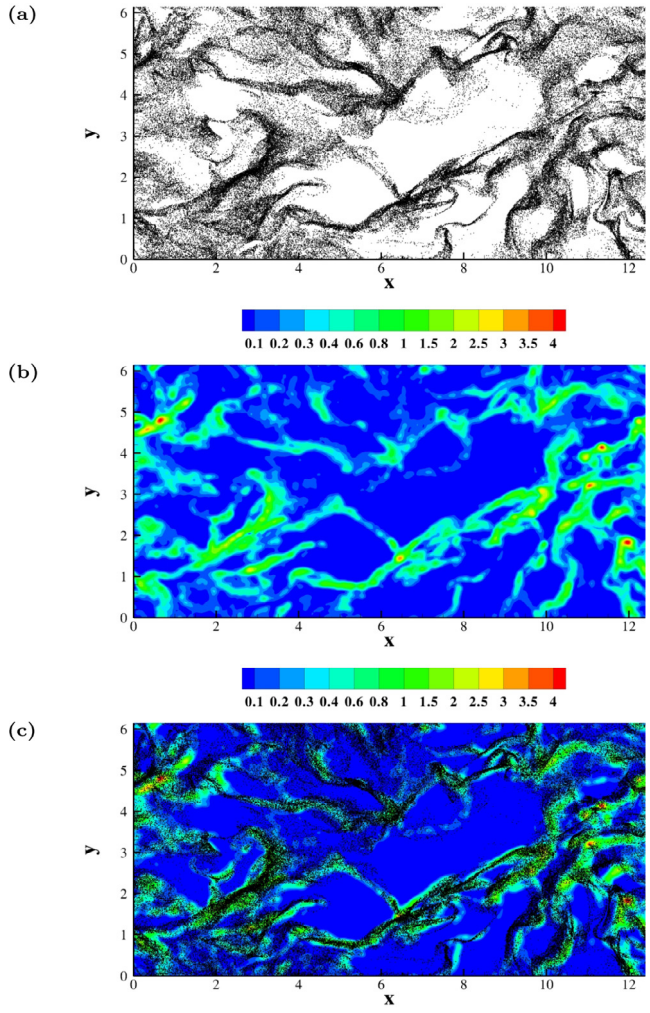

Fig. 2. Snapshot of the instantaneous particle configuration (scatter plot) and of the Eulerian intensity of the force-feedback field operated by the particles on the fluid (contour plot). The slice in the $x-y$ plane has a thickness of the order of few Kolmogorov scales. The mean flow $U(y) = Sy$ in the $x-y$ plane is from left to right. Panel a): scatter plot of the instantaneous particle configuration. Panel b): Eulerian force-feedback field intensity on the fluid. Panel c): instantaneous particle configuration superimposed on the corresponding feedback field.

rameter determines the extension of the range of scales below the shear scale L_S and above the Kolmogorov length η where turbulent fluctuations are driven by (non-linear) inertial energy transfer mechanisms. When this range is sufficiently extended, i.e. the Taylor-Reyolds number is large enough, small scale isotropy recovery is likely to occur in the fluid velocity field. The shear strength, defined as $S^* = S\langle u_i u_i\rangle/\epsilon = (L_0/L_S)^{2/3}$ where L_0 is the integral scale, fixes the range of scales where fluctuations are driven by the anisotropic turbulent kinetic energy production mechanisms associated with the mean velocity gradient.

With regards to the disperse phase, the Stokes number $St_\eta = \tau_p/\tau_\eta$, defined as the ratio between the particle relaxation time scale $\tau_p = \left(\rho_p/\rho_f\right)d_p^2/18\nu$ and the Kolmogorov timescale τ_η, is well known to control the clustering dynamics. In the two-way coupling regime, other parameters come into play: the mass loading $\Phi = M_p/M_f$ defined as the ratio between the mass of the disperse phase $M_p = \rho_p V_p$ and the carrier fluid $M_f = \rho_f V_f$. The mass fraction can be expressed as $\Phi = (\rho_p/\rho_f)\Phi_V$. In the definition of the volume fraction $\Phi_V = V_p/V_f, \quad V_p = N_p \pi \rho_p d_p^3/6$ is the volume occupied by the N_p particles in the fluid volume V_f. The density ratio ρ_p/ρ_f is assumed to be much larger than unity to achieve appreciable loads even in dilute suspensions. In summary, the dimensionless quantities $\{S^*, Re_\lambda, St_\eta, \Phi, N_p\}$ are the physical parameters which control the dynamics of two-way coupled multiphase flows in the asymptotic conditions $d_p \ll \eta$, $\rho_p \gg \rho_f$ and $\Phi_V \ll 1$.

In the context of homogeneous shear flow, Eqs. (12) are solved exploiting the Rogallo's algorithm, (Rogallo, 1981). The instantaneous velocity field is decomposed as the sum of mean and fluctuation, $\mathbf{u} = Sx_2\,\mathbf{e}_1 + \mathbf{u}'$. Rogallo's technique is then employed to write the Navier–stokes equations for velocity fluctuations in a coordinate system convected by the mean flow according to the transformation of variables $\xi_1 = x_1 - St\,x_2$; $\xi_2 = x_2$; $\xi_3 = x_3$; $\tau = t$. In computational space, the equation for $\mathbf{u}'$ turns out to be homogeneous since the non-homogeneous term $\mathbf{U}\cdot\nabla\mathbf{u}'$ is absorbed by the variable transformation which, however, introduces time dependent differential operators $\nabla = (\partial_{\xi_1}, \partial_{\xi_2} - S\tau\,\partial_{\xi_1}, \partial_{\xi_3})$. Due to homogeneity, the Fourier transform can be taken at the cost of dealing with time-dependent wave-numbers $\mathbf{k} = (k_1, k_2 - S\tau\,k_1, k_3)$. Rogallo's transformation allows the use of standard pseudo-spectral methods. The equation for the Fourier coefficients of $\mathbf{u}'$ is integrated in time by a low-storage Runge–Kutta method whilst non-linear terms are evaluated in physical space. Care is taken to control aliasing errors by the standard 3/2 dealiasing rule. The divergence-free constraint leads to a Poisson equation for the pressure that is solved in closed analytical form in Fourier space. Further details can be found in Gualtieri et al. (2002).

The simulations matrix is reported in Table 1 together with the relevant parameters needed to characterize each simulation. The dataset is organized into four sections. The first three entries of the table, A_1, B_1 and C_1, provide cases where the mass loading is changed at fixed Stokes number. In these simulations, the number of particles N_p follows once Φ, St_η and ρ_p/ρ_f are fixed to the desired values. N_p turns out to be smaller than the number computational cells N_c used for the numerical solution of the carrier phase. The following three entries, A_2, B_2 and C_2, serve as a comparison at the same values of Φ and St_η but with the ratio N_p/N_c intentionally fixed to one. Given this additional numerical constraint, the desired mass loading and Stokes number can be achieved only at the expense of the density ratio ρ_p/ρ_f, which has unlikely values, at least for cases A_2 and B_2. However, the latter are the conditions in which one should work in the context of the Particle In Cell (PIC) approach where the additional numerical constraint of $N_p/N_c \simeq 1$ is mandatory to trust in the physical results. Since the number of particles in the ERPP approach can be changed with no negative consequence, cases A_2, B_2 and C_2 serve only for comparison to assess the independency of the results from the average number of particles per cell. Case B_3 provides the grid refinement of case B_1 – the grid spacing is reduced ($Dx/\eta = 0.5$) for a fixed regularization scale ($\sigma_R/\eta = 1$). In case B_4, the grid is refined as in case B_3 and the regularization length-scale is now smaller than the Kolmogorov scale ($\sigma_R/\eta = 0.5$). The last six entries of the table – *D, E, F,* E_1, E_2 and E_3 – provide data at relatively higher Reynolds number and at different Stokes numbers. Note that the conditions in terms of the Stokes number and/or mass loading are similar to those occurring in technological applications. For instance, in a typical diesel engine, see e.g. (Ferguson and Kirkpatrick, 2015), the mass of fluid injected per cycle per cylinder is about $3\cdot10^{-4}$ kg. Considering a four stroke, 2.5 litre engine with 4 cylinders, back of the envelope calculations immediately give a mass loading of approximately 0.4 and a volume fraction of the order $\phi_V = 6\cdot10^{-3}$. In modern common-rail injection systems, the diameter of the droplets is about $d_p = 1 \div 10\,\mu$m whilst the Kolmogorov scale is of the order $\eta = 30\mu$m. In these conditions, the Kolmogorov Stokes number ranges from 0.05 up to 5 and overlaps the range of values addressed in this paper.

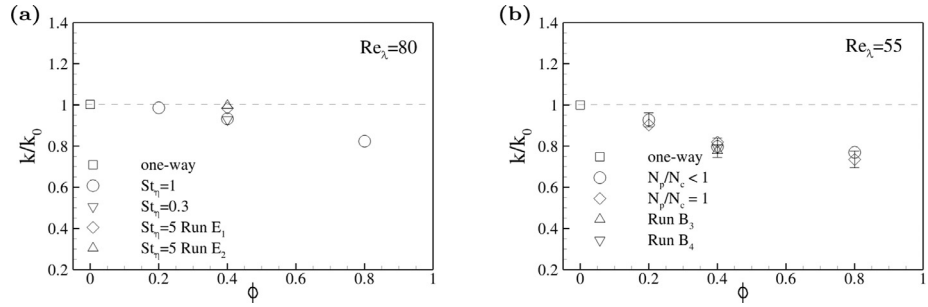

Fig. 3. Normalized turbulent kinetic energy k/k_0 versus the mass loading Φ for different values of the Stokes number. Panel a): simulations at $Re_\lambda = 80$. Uncoupled case (□); $St_\eta = 1$ (◯); $St_\eta = 0.3$ (▽); $St_\eta = 5$ (◇), run E_1; $St_\eta = 5$ (△), run E_2. Panel b): simulations at $Re_\lambda = 55$. Runs A_1, B_1 and C_1 with $N_p/N_c < 1$ (◯) are compared against A_2, B_2 and C_2 with $N_p/N_c = 1$ (◇). Run B_3 (△) provides the grid refinement of case B_1 with $\sigma_R/\eta = 1$ and $Dx/\eta = 0.5$. Case B_4 (▽) checks the sensitivity of the regularization length-scale, $\sigma_R/\eta = 0.5$. Error-bar height is $2\sigma/\sqrt{N_s}$ where σ is the variance associated to the averaged data and N_s is the number of samples used to compute averages.

Each simulation is initialized by exploiting an already fully developed turbulent field achieved by a companion simulation. The particles are initially homogeneously distributed in space with velocity matching the fluid velocity at their positions. After discarding an initial transient, 300 uncorrelated snapshots for the simulations operated on the finest grids up to 600 and 900 snapshots for the intermediate and coarser grids respectively are stored every $T_{stat}/\tau_0 = 2$ where τ_0 is the large scale correlation time of the flow, i.e. the integral timescale.

An instantaneous field of the particle-laden turbulent flow is reported in Fig. 2. The panels represent a cut of the three dimensional field in an $x-y$ plane containing the mean flow. The data refers to case E of Table 1 where $St_\eta = 1$ and $\Phi = 0.4$. Panel a) shows a snapshot of the particles configuration and panel b) reports the corresponding Eulerian feedback field on the fluid. As apparent from the instantaneous particle configuration, the presence of the mean flow dramatically gives a preferential spatial orientation to the particle aggregates, referred to as clusters. It is well known that in the conditions of unitary Stokes number, the clusters form a multi-scale geometrical set. As discussed in the literature, the clustering phenomena occurs at the smallest scales. Such behavior is crucial in the two-way coupling regime where the cluster geometry fixes the sets where the back-reaction field acts on the fluid. These ideas can be still visualized in Fig. 2 by correlating the instantaneous particle configuration to the intensity of the feedback field. Panel c) reports the superposition of panel a) and b). The instantaneous Eulerian feedback field on the fluid retains the same geometrical features of the clusters, i.e. the back-reaction on the fluid is a multi-scale field which forces turbulent fluctuations in a wide range of spatial scales spanning from the integral scale, which is comparable to the cluster length, to the Kolmogorov scale, which is comparable to the cluster width. Panel b) shows that the field is smooth and well resolved even though the average number of particles per cell for case E is pretty small, about 0.1. Indeed, the feedback kernel is regular everywhere once the regularization length-scale σ_R is resolved on the computational grid.

3.2. Turbulent kinetic energy

Panel a) of Fig. 3 reports the turbulent kinetic energy k as a function of the mass loading Φ for cases D, E and F at $St_\eta = 1$. The data for cases E_1, E_2 and E_3 at different Stokes number – $St_\eta = 0.3$ and $St_\eta = 5$ – have also been reported. The turbulent kinetic energy is normalized with the corresponding value k_0 in the unladen case (no feedback on the fluid). Consistently with available data in the literature for homogeneous isotropic turbulence and homogeneous shear flow, as the mass loading is increased the kinetic energy is attenuated for particles at $St_\eta = 1$. Particles at $St_\eta = 0.3$ behave as the population at $St_\eta = 1$ for $\Phi = 0.4$ while heavier particles at $St_\eta = 5$ leave the kinetic energy almost unchanged. In this last case, there is no appreciable effect of the density ratio on the results, compare run E_1 and E_2. Panel b) reports the turbulent kinetic energy versus the mass loading for the simulations at $Re_\lambda = 55$. The data shows that i) the results are independent of the number of particles per cell; ii) the solution is grid convergent and iii) the physical results do not depend from the value of the regularization length-scale. Statement i) is supported by the comparison between cases A_1, B_1, C_1 and A_2, B_2, C_2. The former cases have few particles per cell while the latter share $N_p/N_c = 1$. Within statistical accuracy, quantified by the error-bars in the plot corresponding to $2\sigma/\sqrt{N_s}$, where σ is the variance associated with the averages and N_s is the number of samples used to compute averages, the data shows that the turbulent kinetic energy is independent on how many particles per cell are available. Indeed, in the ERPP approach, the number of particles N_p can be safely changed to cope with the actual physical conditions, with no negative effect on the results. In panel b), run B_3 provides the grid refinement check – the number of grid points has been doubled in each direction – for the reference case B_1 with $\sigma_R = \eta$. As expected, doubling the number of grid points provides a better numerical representation of the same physical solution even though the ratio N_p/N_c becomes almost one order of magnitude smaller, thus supporting once more statements i) and ii). Case B_4 shows the convergence with respect the regularization length-scale that is now smaller than the Kolmogorov scale $\sigma_R/\eta = 0.5$, see statement iii) and the extended discussion in Gualtieri et al. (2017).

3.3. Energy and dissipation spectra

The energy spectrum, when compared to the uncoupled case, shows the scales of turbulence which are affected by the back-reaction. Panel a) of Fig. 4 shows the energy spectrum for three cases, D, E and F, which differ in mass loading with $\Phi = 0.2, 0.4, 0.8$ at a fixed Stokes number $St_\eta = 1$. Data sets at $St_\eta = 0.3$ and $St_\eta = 5$, at fixed mass loading $\Phi = 0.4$, are also shown, see cases E_1, E_2 and E_3. Comparing cases D, E and F, the energy content of the largest scales is slightly decreased while the smallest scales are progressively energized as Φ is increased. Panel b) shows the corresponding dissipation spectrum which better highlights the alteration of turbulence at the smallest scales that are significantly energized by the back-reaction when compared to the uncoupled case. This behavior is likely due to the high clustering intensity that occurs at $St_\eta = 1$. The particle clusters are extremely elongated (length of the order of the integral scale) and tiny (thickness of the order of the Kolmogorov scale). As a consequence, the spectrum of the back-reaction spans the entire range of resolved scales. Note however how the energy spectrum and the dissipation spectrum nicely behave at smallest scales, i.e. at the highest wave numbers.

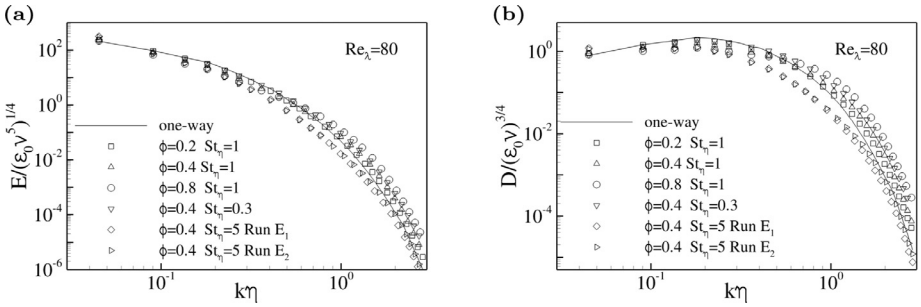

Fig. 4. Energy spectrum (panel a) and dissipation spectrum $D = 2\nu k^2 E$ (panel b) versus wavenumber k at $Re_\lambda = 80$ for different cases. Data normalized in Kolmogorov units with ϵ_0, the energy dissipation rate in the uncoupled case. Uncoupled case (solid line); $\Phi = 0.2$, $St_\eta = 1$ (□); $\Phi = 0.4$, $St_\eta = 1$ (△); $\Phi = 0.8$, $St_\eta = 1$ (◯); $\Phi = 0.4$, $St_\eta = 0.3$ (▽); $\Phi = 0.4$, $St_\eta = 5$ (◇), run E_1; $\Phi = 0.4$, $St_\eta = 5$ (▷), run E_2.

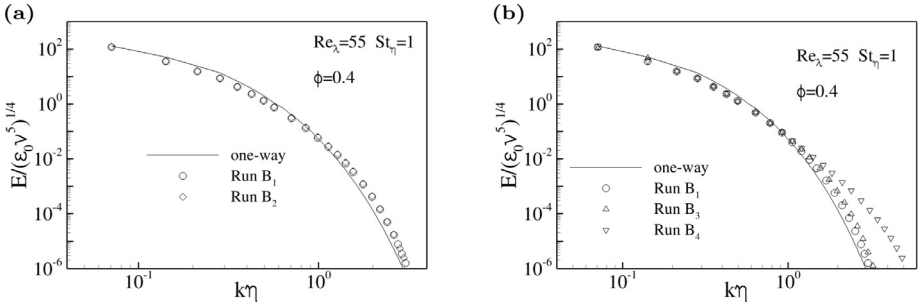

Fig. 5. Energy spectrum versus the wavenumber k at $Re_\lambda = 55$. Data are made dimensionless in Kolmogorov units. Panel a): data at the fixed mass loading $\Phi = 0.4$ and Stokes number $St_\eta = 1$ are compared when the average number of particles per cell is changed – run B_1 and run B_2 of Table 1. Panel b): reference data at given mass loading $\Phi = 0.4$ and Stokes number $St_\eta = 1$, run B_1 (◯), are compared against data obtained on a finer grid, run B_3 (△) at a fixed value of the ratio $\sigma_R/\eta = 1$. Data pertaining to run B_4 (▽) is also reported to check the sensitivity to the change of the regularization length-scale – $\sigma_R/\eta = 0.5$.

This is a consequence of the proper regularization of the feedback field. In panel a), the data for cases E_1, E_2 and E_3 show the effect of the Stokes number, $St_\eta = 0.3$, and for the case at $St_\eta = 5$ also the effect of the density ratio, on the turbulence alteration when the mass loading is kept fixed. Particles with $St_\eta = 0.3$ show a similar behavior with respect to the population at $St_\eta = 1$. This is related to the fact that particles at $St_\eta = 0.3$ are still characterized by small-scale clustering similarly to particles at $St_\eta = 1$. Heavier particles at $St_\eta = 5$, which are less affected by the small-scale clustering, irrespective of the density ratio, produce a completely different alteration of the turbulent fluctuations. Specifically, the turbulent energy spectrum is depleted at all scales except for the first few modes which are augmented. This is a direct consequence of the augmented particle inertia. At increasing Stokes number, the particles are responsive only to the largest scales of the flow and the threshold where turbulence is augmented/depleted shifts towards the largest scales. This behavior is consistent with the overall increase of the turbulent kinetic energy discussed in the previous section. The effect of the Stokes number on the dissipation spectrum is shown in panel b).

As reported in panel a) of Fig. 5, the energy spectrum for cases B_1 and B_2 at $\Phi = 0.4$ and $St_\eta = 1$ shows the same behavior at each resolved scale. Irrespective of the number of particles per computational cell N_p/N_c, the ERPP approach provides a physically consistent and smooth regularization of feedback force on the fluid. Panel b) compares the data at $\Phi = 0.4$ and $St_\eta = 1$ obtained on a finer grid, run B_3, against the reference data of run B_1, showing the grid-convergence properties of the ERPP method. In panel b), run B_4, obtained on a finer grid with a smaller regularization length-scale $\sigma_R = 0.5\eta$, is reported showing that by reducing σ_R the scales shared among different cases are not affected by the regularization parameter, see the discussion in Gualtieri et al. (2017).

Fig. 6 shows the comparison between the ERPP and Particle In Cell (PIC) approaches. The energy and dissipation spectra are shown in panels a) and b) respectively for the same physical conditions of $\Phi = 0.8$ and $St_\eta = 1$. Note how, in the PIC approach, the high wave-number tail of the energy spectrum and more evidently of the dissipation spectrum is strongly affected by N_p/N_c. A detailed discussion about the difficulties related to N_p/N_c when using the PIC method is reported in Gualtieri et al. (2013). The corresponding high wave-number range in the ERPP approach confirms that the number of particles N_p can be safely changed irrespective of N_c. The approach therefore allows any mass loading for a fixed Stokes number and density ratio, see (Gualtieri et al., 2015) for a preliminary discussion on this idea which is now demonstrated by the present results.

3.4. Anisotropic turbulence modification

This subsection documents the anisotropic alteration of the turbulent flow. Fig. 7 shows some selected single point statistics. Panel a) reports the velocity variance in the streamwise direction $\langle u_1^2 \rangle$ and panel b) reports the velocity variance along the direction of the mean shear $\langle u_2^2 \rangle$ as a function of the mass loading Φ. The data has been normalized by the corresponding values in the uncoupled case. Particles at $St_\eta = 1$ do not significantly change the value of the streamwise velocity variance whilst they attenuate the velocity fluctuations in the shear direction. Lighter particles, say at $St_\eta = 0.3$, do not appreciably change the velocity variances in the streamwise or shear directions. A more interesting modification is produced by heavier particles at $St_\eta = 5$. In these cases, the velocity variance in the streamwise direction is augmented with respect to the uncoupled case while the velocity variance in the shear direction is attenuated, as seen for particles at $St_\eta = 1$. This behavior can be attributed to the particle inertia. As the Stokes number increases, a ballistic regime is progressively approached where the particles filter out the small scale fluid velocity fluctuations and retain only the turbulent fluctuations at the largest scales. The

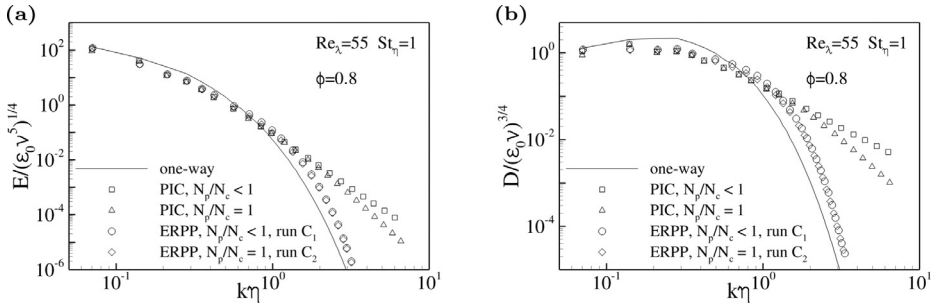

Fig. 6. Energy spectrum (panel a) and dissipation spectrum $D = 2\nu k^2 E$ (panel b) versus wavenumber at $Re_\lambda = 55$, mass loading $\Phi = 0.8$ and Stokes number $St_\eta = 1$. Data normalized in Kolmogorov units. Results from the ERPP method (◯, ◇) are compared against corresponding data obtained from the Particle In Cell method (□, △). Cases with few particles per cell, ERPP (◯) and PIC (□). Cases with $N_p/N_c = 1$, ERPP (◇) and PIC (△).

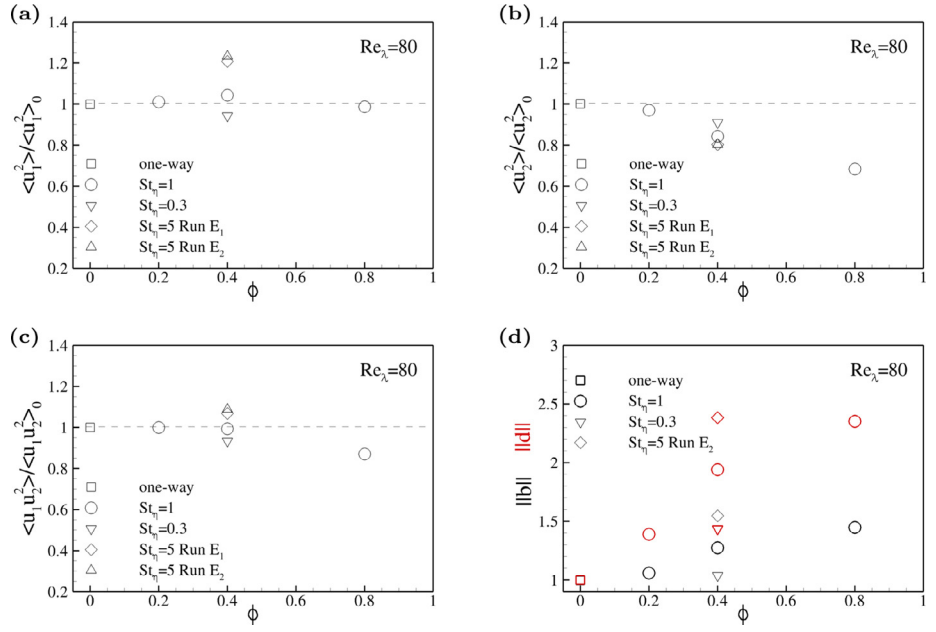

Fig. 7. Panel a): velocity variance in the streamwise direction. Panel b): velocity variance along the shear direction. Panel c): Reynolds shear stresses. Panel d): norm of the deviatoric component of the Reynolds stress tensor (black symbols) and norm of the deviatoric component of the pseudo-dissipation tensor (red symbols), see text for definitions. Data normalized with corresponding values in the uncoupled case, denoted with the subscript, are plotted versus the mass loading Φ for the available Stokes number at $Re_\lambda = 80$. Uncoupled case (□); $St_\eta = 1$ (◯); $St_\eta = 0.3$ (▽); $St_\eta = 5$ (◇) run E_2. (For interpretation of the references to color in this figure legend, the reader is referred to the web version of this article.)

particle velocity is therefore expected to be different with respect to the fluid velocity, giving rise to a more intense force-feedback on the fluid. In the ballistic limit, the particles tend to preserve their velocity, dragging along the fluid and generating larger fluctuations in the streamwise direction with respect to lighter particles. The velocity variance in the spanwise direction (not shown) behaves similarly to $\langle u_2^2 \rangle$. The augmentation of $\langle u_1^2 \rangle$ overwhelms the attenuation of $\langle u_2^2 \rangle$ and $\langle u_3^2 \rangle$ resulting in a slight increase in turbulent kinetic energy, as shown in the previous Section 3.2. Panel c) reports the Reynolds shear stresses $\langle u_1\, u_2 \rangle$ which are responsible for the turbulent kinetic energy production rate $\mathcal{P} = -S\langle u_1\, u_2 \rangle$. An overall attenuation of the Reynolds shear stresses is observed when the mass loading is increased for particles at $St_\eta = 1$. Particles with $St_\eta = 0.3$ leave this quantity unchanged while heavier particles at $St_\eta = 5$ produce higher turbulent shear stress. This behavior can again be ascribed to inertial effects. In the low inertia case, particles are responsive to a broader range of fluid time and space fluctuations. They can therefore follow both fluctuations in the streamwise and in the shear direction at the same time, giving rise to a marginal alteration of the shear stresses. In contrast, particles with higher inertia produce a much higher momentum flux since they are responsive only to the largest scales motions. Once the particles move in the direction of the shear they tend to preserve their longitudinal and vertical velocity, generating a sensible shear stress on the fluid.

The results discussed so far highlight that the alteration of turbulence fluctuations is strongly directional, i.e. what happens in the streamwise or cross-flow directions is significantly different. This modification can be globally quantified by the deviatoric component of the Reynolds stress tensor defined as $b_{ij} = \langle u_i\, u_j \rangle / \langle u_k\, u_k \rangle - \frac{1}{3}\delta_{ij}$, where δ_{ij} is the Kronecker symbol. The norm $\|b\| = \sqrt{b_{ij}\, b_{ij}}$, is reported in panel d) for the available data (black symbols). This observable shows that the overall anisotropic content of the largest scales is dramatically enhanced in the two-way coupling regime when the mass loading is increased at fixed Stokes number or when the mass loading is fixed and the Stokes number is increased. The anisotropy level of the smallest scales is characterized by the deviatoric component of the pseudo-dissipation tensor $\epsilon_{ij} = 2\nu \langle \partial_k u_i\, \partial_k u_j \rangle$, namely $d_{ij} = \epsilon_{ij}/\epsilon_{kk} - \frac{1}{3}\delta_{ij}$. The norm $\|d\| = \sqrt{d_{ij}\, d_{ij}}$ is reported in panel d) (red symbols). The effects of the inter-phase momentum exchange is even more striking at the level of the velocity gradients where the anisotropy increase is larger with respect to the anisotropy increase of the largest scales.

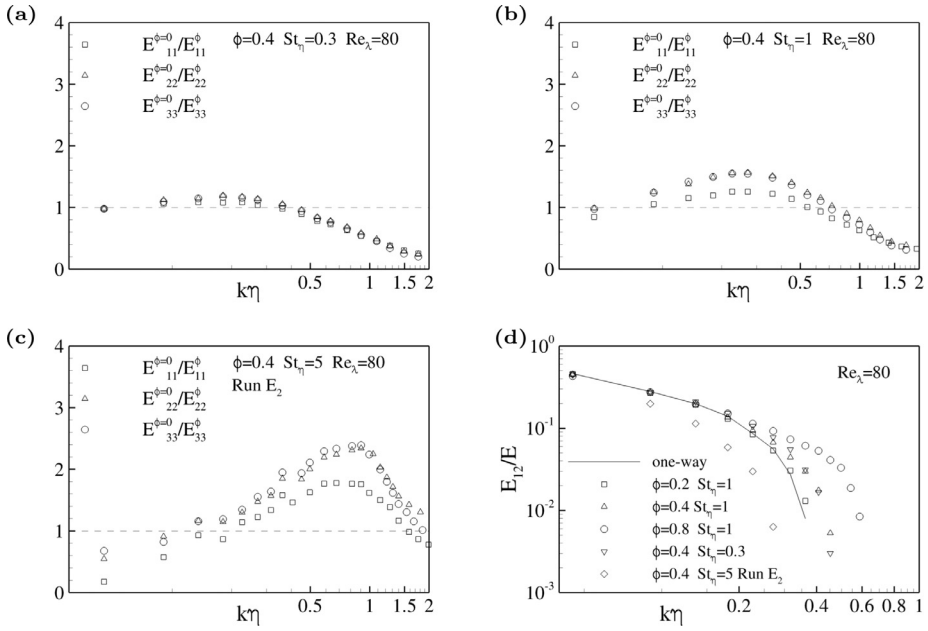

Fig. 8. Ratio $E_{ii}^{\Phi=0}/E_{ii}^{\Phi}$ (no sum on the repeated index i) versus wavenumber. Streamwise direction (□); shear direction (△); spanwise direction (◯); at $\Phi = 0.4$ and different Stokes number, namely $St_\eta = 0.3$ (panel a)); $St_\eta = 1$ (panel b)); $St_\eta = 5$ (panel c)). Panel d): ratio E_{12}/E vs. wavenumber: uncoupled case (solid line); $\Phi = 0.2$, $St_\eta = 1$ (□); $\Phi = 0.4$, $St_\eta = 1$ (△); $\Phi = 0.8$, $St_\eta = 1$ (◯); $\Phi = 0.4$, $St_\eta = 0.3$ (▽); $\Phi = 0.4$, $St_\eta = 5$ (◇), run E_2.

Fig. 8 addresses the anisotropic modification of turbulence in spectral space quantified by the i-th component of the velocity spectrum, namely E_{ii}^{Φ} (no sum on the repeated index i). Panels a), b) and c) show the ratio $E_{ii}^{\Phi=0}/E_{ii}^{\Phi}$ between the energy spectrum in the uncoupled case and in presence of backreaction, for different values of the Stokes number at fixed mass loading $\Phi = 0.4$. Different velocity components are reported with different symbols. Starting from light particles, $St_\eta = 0.3$, turbulence is energized at the smallest scales while only a slight modification is observed at the largest scales. Particles at $St_\eta = 1$ produce an appreciable attenuation of the energy contents of the largest scales. The level of attenuation/augmentation among the three velocity components appears to be different. For instance, at large scales, the population at $St_\eta = 1$ induces a slight depletion of the streamwise spectrum while the depletion in the cross-flow direction is almost double. Moving towards the smallest scales, all three components are almost equally augmented. Heavier particles at $St_\eta = 5$, case E_2, generate a completely different modification of the turbulent fluctuations. The spectrum is attenuated in almost the whole range of resolved scales with the effect being largest at the dissipative scales. In contrast, at the largest scales, the spectrum is augmented consistently with the fact that the turbulent kinetic energy and the velocity variances result globally augmented in this case. Note that the three velocity components are affected in a different manner, thus enhancing the overall level of the flow anisotropy at each scale. Panel d) addresses the ratio between the energy co-spectrum and the energy spectrum. This indicator vanishes in isotropic conditions and can be assumed to measure the relative anisotropic energy content of each scale, see e.g. the seminal paper by Saddoughi and Veeravalli (1994). From the data, it emerges that in the two-way coupling regime the range of scales affected by anisotropy is progressively larger as the mass loading is increased, at least for particles with $St_\eta = 1$. For unitary Stokes number, the particle clusters span from the Kolmogorov to the integral scale and, as apparent from the instantaneous plots and confirmed by statistical analysis, the clusters retain a preferential orientation induced by the mean flow up to the smallest scales. This implies that the spatial support of the feedback field on the flow is anisotropic and forces the fluid in specific directions. In contrast, heavier particles at $St_\eta = 5$ deplete the anisotropy content at the fixed mass loading of $\Phi = 0.4$. In fact, at increasing inertia small scale clustering is attenuated and the support of the feedback field looses its directionality. Moreover, due to ballistic effects, the particle motion becomes less correlated to the fluid motion, hindering the possibility to achieve a coherent forcing on the fluid in a specific direction.

As evident from the results presented up to this point, the presence of particles strongly alters the turbulent fluctuations throughout the resolved range of scales. The smallest scales are also affected by the backreaction in a non-trivial way. One of the distinctive features of turbulence is the presence of rare and intense velocity fluctuations at the different scales, known as intermittency, see e.g. (Frisch, 1996). A possible measure of intermittency is provided by the statistical behavior of the random variable represented by the longitudinal velocity increments. Given two points in space, $\mathbf{x}$ and $\mathbf{y}$, it is possible to measure the velocity difference $\delta u = [\mathbf{u}(\mathbf{y}) - \mathbf{u}(\mathbf{x})] \cdot \hat{\mathbf{r}}$ where $\hat{\mathbf{r}}$ is the unit vector joining the points $\mathbf{y}$ and $\mathbf{x}$. This observable can be measured for each separation r. Panel a) of Fig. 9 shows the probability distribution function (PDF) of the random variable $\delta u(r)$ evaluated at a separation $r\eta = 2$ (small scales). Different data sets are reported and compared to the reference, uncoupled case. It seems that the fluid velocity fluctuation statistics at the small scales are sensibly different from a Gaussian distribution. This means that intense fluctuations are likely to occur in turbulent flow as can be seen by the tails of the PDF. In the case of two-way coupled simulations, the presence of the particles modify the statistics of the turbulent fluctuations at the smallest scales. As the mass loading is increased, the rare and intense events that already characterize the unladen flow become even more important, as shown by the fact that the PDF is broadened and the tails decay slower than the reference uncoupled case. In other words, the presence of the particles triggers extremely rare events that are unlikely to occur in the uncoupled case. For instance, the frequency of events at five times the variance is increased by one order of magnitude. A scale-dependent measure of the intermittency is provided by the flatness of the PDF, namely $F(r) = \langle \delta u^4 \rangle / \langle \delta u^2 \rangle^2$, that is shown as a function of the separation in panel b). The interesting point is that in turbulence, the flatness is a quantity that is scale-dependent, meaning that statistics

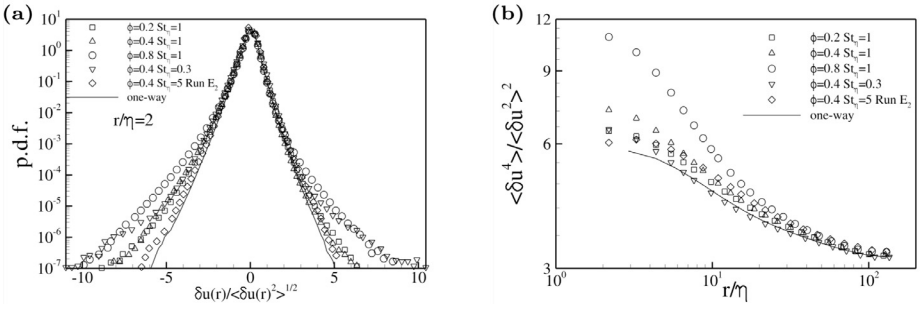

Fig. 9. Panel a): probability density function of the longitudinal velocity increments at separation $r/\eta = 2$. Panel b): flatness of the velocity increments versus separation. $\Phi = 0.2$, $St_\eta = 1$ (□); $\Phi = 0.4$, $St_\eta = 1$ (△); $\Phi = 0.8$, $St_\eta = 1$ (◯); $\Phi = 0.4$, $St_\eta = 0.3$ (▽); $\Phi = 0.4$, $St_\eta = 5$ (◇), run E_2.

of the velocity increments do not follow the dimensional prediction. Following Kolmogorov K41 theory, the moments of the longitudinal velocity increments can be described by dimensional arguments by the scaling laws $\langle \delta u^p \rangle \propto \epsilon^{p/3} r^{p/3}$ which evidently give a scale independent flatness. In turbulence, the scaling laws depart from the dimensional prediction and follow a power law behavior $\langle \delta u^p \rangle \propto r^{\zeta_p}$, where the scaling exponents ζ_p are a nonlinear convex function of p. In particular, the flatness as a function of the separation should scale as $F \propto r^{\zeta_4 - 2\zeta_2}$. This function increases as the separation is reduced, given the fact that the scaling exponents do not follow the dimensional prediction implying that $\zeta_4 < 2\zeta_2$. The flatness shown in panel b) highlights how, in presence of the particles, the flatness is modified throughout the range of scales. The flatness diverges faster at small scales as the mass loading is increased. This behavior suggests that the backreaction is able to modify the hierarchy of the scaling exponents towards an overall increase in intermittency. In all cases, Gaussian statistics are recovered at the largest scales comparable to the integral scale, where the flatness approaches the value of three and the corresponding PDF of the velocity increments (not shown) is well fitted by a Gaussian function.

4. Final remarks

We have applied the ERPP method to the direct numerical simulation of turbulent flows in the two-way coupling regime with up to millions of sub-Kolmogorov particles.

The simulations in the homogeneous shear flow were instrumental to address the turbulence modulation induced by small inertial particles at different mass loadings and Stokes numbers. Turbulence intensities are selectively altered by the presence of the disperse phase. The streamwise velocity fluctuations are almost unaltered when the mass loading is changed for small inertia particles, such as $St_\eta \leq 1$. In contrast, large inertia particles at $St_\eta = 5$ augment the streamwise velocity fluctuations. Irrespective of the Stokes number, the crossflow velocity variances are attenuated at increased mass loading. This selective turbulence modification impacts the anisotropic content of both the large and small scales.

The scale-by-scale turbulence modulation has been addressed by inspecting the energy spectrum, the cospectrum and the dissipation spectrum. The effects of the momentum coupling at increasing mass loading and at unitary Stokes number results in an attenuation of the energy content of the largest scales and an amplification at the smallest ones. Small inertia particles have less effect on the scale-by-scale energy content while particles with larger inertia attenuate the energy content at almost each wavenumber whilst the energy content of the first few modes is augmented. Even at the level of two-point statistics, such as the energy spectrum and cospectrum, the alteration is selective. The energy cospectrum is progressively broadened when increasing the mass loading, showing that the back-reaction forces anisotropic modes in the system. The same conclusion is reached by inspection of the spectrum pertaining the three velocity components. At small scales, the spectrum of the velocity components is augmented. At the largest scales, the attenuation of the velocity fluctuations in the spanwise and shear direction is more pronounced with respect to the modification of the streamwise fluctuation which remains almost unaltered. Interestingly, the probability density function of the longitudinal velocity increments measured at the Kolmogorov scale shows a sensible broadening with respect to the reference one-way coupling case. It follows that the probability to observe rare and intense events, i.e. intermittency, is increased by the particle backreaction as shown throughout the range of scales by the corresponding flatness.

The results show that the ERPP method is able to tackle uneven flow conditions where $N_p/N_c \ll 1$ since the perturbation field generated by each particle is smooth and the regularization procedure does not depend on the grid spacing.

Finally, it is noteworthy to comment on applications where the turbulent flow is laden with heavy particles, say $St_\eta \gg 1$. To give an example, the process of inter-particle collisions, (Pan and Padoan, 2014), and turbulence modification, (Fu et al., 2014; Johansen et al., 2007), play a crucial role in the astrophysical context where the correct prediction of the time required for the formation of a protoplanet in an accretion disk is still an open issue, (Mitra et al., 2013). In such context, the Stokes number might span several orders of magnitude. Let us consider a hydrogen gas accretion disk that can be modeled as a turbulent shear flow due to the fast rotation. From the data available in the literature, the Stokes number ranges from $5 \cdot 10^{-2}$ to $5 \cdot 10^3$. Given the very large values of the density ratio, the particles are small compared to η. In these conditions, i.e. $St_\eta = 5 \cdot 10^3$, a simulation at the Reynolds number presented in the paper would require very few particles per computational cell, namely $N_p/N_c = 0.001$. This simulation would only be possible in the ERPP framework where the small number of particles per cell is not an issue.

The research has received funding from the European Research Council under the ERC Grant Agreement no. 339446. We acknowledge PRACE-2IP project (FP7 RI-283493) resource *Zeus* based in Poland at Krakow. We acknowledge the CINECA award under the ISCRA initiative (project HP10BFQSTY), for the availability of high performance computing resources and support.

References

Akiki, G., Jackson, T.L., Balachandar, S., 2017. Pairwise interaction extended point–particle model for a random array of monodisperse spheres. J. Fluid Mech. 813, 882–928.

Balachandar, S., Eaton, J.K., 2010. Turbulent dispersed multiphase flow. Ann. Rev. Fluid Mech. 42, 111–133.

Balachandar, S., Maxey, M.R., 1989. Methods for evaluating fluid velocities in spectral simulations of turbulence. J. Comput. Phys. 83, 96–125.

Battista, F., Picano, F., Troiani, G., Casciola, C.M., 2011. Intermittent features of inertial particle distributions in turbulent premixed flames. Phys. Fluids 23 (12), 123304.

Bec, J., Biferale, L., Cencini, M., Lanotte, A., Musacchio, S., Toschi, F., 2007. Heavy particle concentration in turbulence at dissipative and inertial scales. Phys. Rev. Fluids 98 (8), 084502.

Boivin, M., Simonin, O., Squires, K.D., 1998. Direct numerical simulation of turbulence modulation by particles in isotropic turbulence. J. Fluid Mech. 375, 235–263.

Calzavarini, E., Kerscher, M., Lohse, D., Toschi, F., 2008. Dimensionality and morphology of particle and bubble clusters in turbulent flow. J. Fluid Mech. 607, 13–24.

Capecelatro, J., Desjardins, O., 2013. An euler–lagrange strategy for simulating particle-laden flows. J. Comput. Phys. 238, 1–31.

Caporaloni, M., Tampieri, F., Trombetti, F., Vittori, O., 1975. Transfer of particles in nonisotropic air turbulence. J. Atmos. Sci. 32 (3), 565–568.

Crowe, C.T., Sharma, M.P., Stock, D.E., 1977. The particle-source in cell method for gas droplet flow. J. Fluids Eng. 99, 325.

Crowe, C.T., Troutt, T.R., Chung, J.N., 1996. Numerical models for two-phase turbulent flows. Ann. Rev. Fluid Mech. 28 (1), 11–43.

Durham, W.M., Climent, E., Barry, M., De Lillo, F., Boffetta, G., Cencini, M., Stocker, R., 2013. Turbulence drives microscale patches of motile phytoplankton. Nature Commun. 4.

Eaton, J.K., 2009. Two-way coupled turbulence simulations of gas-particle flows using point-particle tracking. Int. J. Multiph. Flow 35(9), 792–800.

Elghobashi, S., 1994. On predicting particle-laden turbulent flows. Appl. Sci. Res. 52 (4), 309–329.

Elgobashi, S., 2006. An updated classification map of particle-laden turbulent flows. In: Proceedings of the IUTAM Symposium on Computational Approaches to Multiphase Flow. Springer, pp. 3–10.

Ferguson, C.R., Kirkpatrick, A.T., 2015. Internal Combustion Engines: Applied Thermosciences. John Wiley & Sons.

Ferrante, A., Elghobashi, S., 2003. On the physical mechanisms of two-way coupling in particle-laden isotropic turbulence. Phys. Fluids 15 (2), 315–329. (1994-present)

Frisch, U., 1996. Turbulence: The Legacy of an Kolmogorov. Cambridge University Press.

Fu, W., Li, H., Lubow, S., Li, S., Liang, E., 2014. Effects of dust feedback on vortices in protoplanetary disks. Astrophys. J. Lett. 795 (2), L39.

Garg, R., Narayanan, C., Lakehal, D., Subramaniam, S., 2007. Accurate numerical estimation of interphase momentum transfer in Lagrangian–Eulerian simulations of dispersed two-phase flows. Int. J. Multiph. Flow 33 (12), 1337–1364.

Gatignol, R., 1983. The faxén formulas for a rigid particle in an unsteady non-uniform stokes-flow. J. Mécanique théorique et Appl. 2 (2), 143–160.

Gualtieri, P., Battista, F., Casciola, C.M., 2017. Turbulence modulation in heavy-loaded suspensions of tiny particles. Phys. Rev. Fluids 2 (3), 034304.

Gualtieri, P., Casciola, C.M., Benzi, R., Amati, G., Piva, R., 2002. Scaling laws and intermittency in homogeneous shear flow. Phys. Fluids 14 (2), 583–596.

Gualtieri, P., Picano, F., Casciola, C.M., 2009. Anisotropic clustering of inertial particles in homogeneous shear flow. J. Fluid Mech. 629, 25–39.

Gualtieri, P., Picano, F., Sardina, G., Casciola, C.M., 2013. Clustering and turbulence modulation in particle-laden shear flow. J. Fluid Mech. 715, 134–162.

Gualtieri, P., Picano, F., Sardina, G., Casciola, C.M., 2015. Exact regularized point particle method for multiphase flows in the two-way coupling regime. J. Fluid Mech. 773, 520–561.

Happel, J., Brenner, H., 2012. Low Reynolds Number Hydrodynamics: with Special Applications to Particulate Media, vol. 1. Springer Science & Business Media.

Hoef, M.A.V.d., Annald, M.V.S., Deen, N.G., Kuipers, J.A.M., 2008. Numerical simulations of dense gas-solid fluidized beds: a multiscale modeling strategy. Ann. Rev. Fluid Mech. 40, 47–70.

Horwitz, J., Mani, A., 2016. Accurate calculation of stokes drag for point–particle tracking in two-way coupled flows. J. Comput. Phys. 318, 85–109.

Horwitz, J., Mani, A., 2017. Correction scheme for point-particle two-way coupling applied to nonlinear drag law. Int. J. Multiph. Flow. arXiv: 1703.06966.

Innocenti, A., Marchioli, C., Chibbaro, S., 2016. Lagrangian filtered density function for LES-based stochastic modelling of turbulent particle-laden flows. Physi. Fluids 28 (11), 115106.

Ireland, P.J., Desjardins, O., 2017. Improving particle drag predictions in euler–lagrange simulations with two-way coupling. J. Comput. Phys. 338, 405–430.

Jenny, P., Roekaerts, D., Beishuizen, N., 2012. Modeling of turbulent dilute spray combustion. Progr. Energy Combust. Sci. 38 (6), 846–887.

Johansen, A., Oishi, J.S., Mac Low, M.-M., Klahr, H., Henning, T., Youdin, A., 2007. Rapid planetesimal formation in turbulent circumstellar disks. Nature 448 (7157), 1022–1025.

Lau, T.C.W., Nathan, G.J., 2016. The effect of stokes number on particle velocity and concentration distributions in a well-characterised, turbulent, co-flowing two-phase jet. J. Fluid Mech. 809, 72–110.

Leboissetier, A., Okong'o, N., Bellan, J., 2005. Consistent large-eddy simulation of a temporal mixing layer laden with evaporating drops. part 2. a posteriori modelling. J. Fluid Mech. 523, 37–78.

Li, D., Fan, J., Luo, K., Cen, K., 2011. Direct numerical simulation of a particle-laden low Reynolds number turbulent round jet. Int. J. Multiph. Flow 37 (6), 539–554.

Li, D., Luo, K., Fan, J., 2016. Modulation of turbulence by dispersed solid particles in a spatially developing flat-plate boundary layer. J. Fluid Mech. 802, 359–394.

Longmire, E.K., Eaton, J.K., 1992. Structure of a particle-laden round jet. J. Fluid Mech. 236, 217–257.

Marchioli, C., 2017. Large-eddy simulation of turbulent dispersed flows: a review of modelling approaches. Acta Mech. 228 (3), 741–771.

Marchioli, C., Picciotto, M., Soldati, A., 2007. Influence of gravity and lift on particle velocity statistics and transfer rates in turbulent vertical channel flow. Int. J. Multiph. Flow 33 (3), 227–251.

Marchioli, C., Salvetti, M.V., Soldati, A., 2008. Some issues concerning large-eddy simulation of inertial particle dispersion in turbulent bounded flows. Phys. Fluids 20 (4), 040603.

Marchioli, C., Soldati, A., 2002. Mechanisms for particle transfer and segregation in a turbulent boundary layer. J. Fluid Mech. 468, 283–315.

Marmottant, P., Villermaux, E., 2004. On spray formation. J. Fluid Mech. 498, 73–111.

Maxey, M.R., Riley, J.J., 1983. Equation of motion for a small rigid sphere in a nonuniform flow. Phys. Fluids 26, 2437.

Meneguz, E., Reeks, M.W., 2011. Statistical properties of particle segregation in homogeneous isotropic turbulence. J. Fluid Mech. 686, 338–351.

Meyer, D.W., 2012. Modelling of turbulence modulation in particle-or droplet-laden flows. J. Fluid Mech. 706, 251–273.

Miller, R.S., Bellan, J., 1999. Direct numerical simulation of a confined three-dimensional gas mixing layer with one evaporating hydrocarbon-droplet-laden stream. J. Fluid Mech. 384, 293–338.

Mitra, D., Wettlaufer, J.S., Brandenburg, A., 2013. Can planetesimals form by collisional fusion? Astrophys. J. 773 (2), 120.

Monchaux, R., Bourgoin, M., Cartellier, A., 2010. Preferential concentration of heavy particles: a Voronoi analysis. Phys. Fluids (1994-present) 22 (10), 103304.

Nicolai, C., Jacob, B., Gualtieri, P., Piva, R., 2014. Inertial particles in homogeneous shear turbulence: experiments and direct numerical simulation. Flow Turbul. Combust. 92 (1–2), 65–82.

Nicolai, C., Jacob, B., Piva, R., 2013. On the spatial distribution of small heavy particles in homogeneous shear turbulence. Phys. Fluids 25 (8), 083301.

Okongo, N., Bellan, J., 2004. Part 2 of a computational study of a drop-laden mixing layer. NASA Tech Brief-20110020517.

Olivieri, S., Picano, F., Sardina, G., Iudicone, D., Brandt, L., 2014. The effect of the basset history force on particle clustering in homogeneous and isotropic turbulence. Phys. Fluids 26 (4), 041704.

Pan, L., Padoan, P., 2014. Turbulence-induced relative velocity of dust particles. IV. the collision kernel. Astrophys. J. 797 (2), 101.

Peirano, E., Chibbaro, S., Pozorski, J., Minier, J.-P., 2006. Mean-field/PDF numerical approach for polydispersed turbulent two-phase flows. Progr. Energy Combust. Sci. 32 (3), 315–371.

Picano, F., Sardina, G., Casciola, C.M., 2009. Spatial development of particle-laden turbulent pipe flow. Phys. Fluids (1994-present) 21 (9), 093305.

Picano, F., Sardina, G., Gualtieri, P., Casciola, C.M., 2010. Anomalous memory effects on transport of inertial particles in turbulent jets. Phys. Fluids 22, 0517051.

Pitton, E., Marchioli, C., Lavezzo, V., Soldati, A., Toschi, F., 2012. Anisotropy in pair dispersion of inertial particles in turbulent channel flow. Phys. Fluids (1994-present) 24 (7), 073305.

Poelma, C., Westerweel, J., Ooms, G., 2007. Particle–fluid interactions in grid-generated turbulence. J. Fluid Mech. 589, 315–351.

Post, S.L., Abraham, J., 2002. Modeling the outcome of drop-drop collisions in diesel sprays. Int. J. Multiph. Flow 28 (6), 997–1019.

Reade, W.C., Collins, L.R., 2000. Effect of preferential concentration on turbulent collision rates. Phys. Fluids (1994-present) 12 (10), 2530–2540.

Reeks, M.W., 1983. The transport of discrete particles in inhomogeneous turbulence. J. Aerosol Sci. 14 (6), 729–739.

Rogallo, R.S., 1981. Numerical experiments in homogeneous turbulence. NASA TM-81315.

Saddoughi, S.G., Veeravalli, S.V., 1994. Local isotropy in turbulent boundary layers at high Reynolds number. J. Fluid Mech. 268, 333–372.

Salazar, J.P., De Jong, J., Cao, L., Woodward, S.H., Meng, H., Collins, L.R., 2008. Experimental and numerical investigation of inertial particle clustering in isotropic turbulence. J. Fluid Mech. 600, 245–256.

Sardina, G., Schlatter, P., Picano, F., Casciola, C.M., Brandt, L., Henningson, D.S., 2012. Self-similar transport of inertial particles in a turbulent boundary layer. J. Fluid Mech. 706, 584–596.

Saw, E.W., Shaw, R.A., Ayyalasomayajula, S., Chuang, P.Y., Gylfason, A., 2008. Inertial clustering of particles in high-Reynolds-number turbulence. Phys. Rev. Lett. 100 (21), 214501.

Shotorban, B., Balachandar, S., 2006. Particle concentration in homogeneous shear turbulence simulated via lagrangian and equilibrium Eulerian approaches. Phys. Fluids 18, 065105.

Soldati, A., Marchioli, C., 2009. Physics and modelling of turbulent particle deposition and entrainment: review of a systematic study. Int. J. Multiph. Flow 35(9), 827–839.

Toschi, F., Bodenschatz, E., 2009. Lagrangian properties of particles in turbulence. Ann. Rev. Fluid Mech. 41, 375–404.

Vreman, A.W., 2007. Turbulence characteristics of particle-laden pipe flow. J. Fluid Mech. 584, 235–279.

Woods, W.A., 2010. Turbulent plumes in nature. Ann. Rev. Fluid Mech. 42, 391–412.

Yoshimoto, H., Goto, S., 2007. Self-similar clustering of inertial particles in homogeneous turbulence. J. Fluid Mech. 577, 275–286.

Young, J., Leeming, A., 1997. A theory of particle deposition in turbulent pipe flow. J. Fluid Mech. 340, 129–159.

Zhao, L.H., Andersson, H.I., Gillissen, J.J., 2010. Turbulence modulation and drag reduction by spherical particles. Phys. Fluids (1994-present) 22 (8), 081702.